ADVANCED QUANTUM TECHNOLOGIES
www.advquantumtech.com

Ferromagnetism Induced by Magnetic Dilution in Van der Waals Material Metal Thiophosphates

Jin Peng, Xinyu Yang, Ziye Lu, Lin Huang, Xiyu Chen, Miao He, Jingdong Shen, Yu Xing, Meifeng Liu, Zhe Qu, Zhicheng Wang, Linglong Li, Shuai Dong, and Jun-Ming Liu*

Metal thio(seleno) phosphates MPX_3 attract considerable attention with potential application in spintronics and other types of devices. Here, ferromagnetism in an Ising type diluted magnetic semiconductor $Fe_{1-x}Zn_xPS_3$ is reported. Bulk single crystals of $Fe_{1-x}Zn_xPS_3$ have been synthesized via chemical vapor transport method and characterized by X-ray diffraction. The weak ferromagnetism associated with spin/cluster spin glass emerges at 30% Zn doping. A nearly static ferromagnetic order is observed in the highly diluted magnets $Fe_{0.1}Zn_{0.9}PS_3$. X-ray photoemission measurements indicate introduction of holes and associated Fe^{3+} in samples with ferromagnetic order. Density functional theory calculations confirm the Ising-type ferromagnetic state in highly diluted compounds with hole doping. The interplay between bound magnetic polarons induces impurity-band-exchange and superexchange interactions can explain the evolution of magnetism with Zn doping. The findings suggest that the magnetic diluted $FePS_3$ system is a candidate for potential applications in magnetic devices, and its quantum mechanism should be explored by using microscopic techniques in the near future.

1. Introduction

2D van der Waals (vdW) materials which refer to layered system stacked by vdW force attracted considerable interest since the successful isolation of single-layer graphene in 2004.[1] Packs of 2D vdW materials including black phosphorus,[2,3] boron nitride,[4–6] transition metal dichalcogenides,[7,8] and so on have been synthesized and studied.[9] Most of them are non-magnetic. However, 2D materials with magnetization are desirable for next-generation information technology. Spin, instead of charge as information vehicle can, effectively reduce energy consumption.[10] In recent years, 2D magnets have become a rapidly growing research field.[11,12] Several groups, such as binary transition metal halides/chalcogenides (CrI_3, VSe_2),[12–14] Mxenes (MnB),[15] ternary transition metal compounds (Fe_3GeTe_2, $MnBi_2Te_4$)[16,17] are extensively studied.[18] Their magnetization can persist down to mono or few layers, which confirms the early established Mermin-Wagner theory.[19] This theorem reveals that long-range magnetic order in 2D systems is forbidden at finite temperature for continuous rotation symmetries. The enhanced thermal fluctuations make symmetry-breaking order unsustainable. However, it can be stabilized by gapping the low-energy modes through the introduction of anisotropy, such as in 2D Ising system. Basically, magnetic phenomenon is explained in the frame of crystal field effect, exchange interaction, spin-orbital coupling, and Zeeman effect. In 2D magnets, due to quantum confinements, lower coordination numbers, and strong anisotropic exchange effects, their magnetism may behave different with traditional 3D magnets.

Metal thio(seleno)phosphates MPX_3 (M = transition metal, X = S or Se) is an influential group of 2D vdW materials with magnetization since their intermediate band gaps of 1.3–3.5 eV.[20] They are widely employed for application in spintronic devices, catalysis, field effect transistors, photodetectors, chemical sensors, and energy storage devices.[21] Compositions with different transition metal occupied M site share similar crystal structure with monoclinic space group $c2/m$ as shown in **Figure 1**a.[22] Each transition metal is surrounded by six sulfur or selenium ions, forming a trigonal distorted octahedron. Six edge-shared octahedral forms a honeycomb network. P-P dimers are located at the

J. Peng, X. Yang, Z. Lu, X. Chen, J. Shen, Y. Xing, Z. Wang, L. Li, S. Dong
School of Physics
Southeast University
Nanjing 211189, China
E-mail: sdong@seu.edu.cn

L. Huang, J.-M. Liu
Laboratory of Solid State Microstructures
Nanjing University
Nanjing 210093, China

X. Chen, M. Liu
Institute for Advanced Materials
Hubei Normal University
Huangshi 435002, China

M. He, Z. Qu
Anhui Key Laboratory of Condensed Matter Physics at Extreme Conditions, CAS Key Laboratory of Photovoltaic and Energy Conservation Materials, High Magnetic Field Laboratory of Chinese Academy of Sciences (CHMFL), HFIPS
Chinese Academy of Sciences
Hefei 230031, China

M. He, Z. Qu
Science Island Branch of Graduate School
University of Science and Technology of China
Hefei 230026, China

The ORCID identification number(s) for the author(s) of this article can be found under https://doi.org/10.1002/qute.202200105

DOI: 10.1002/qute.202200105

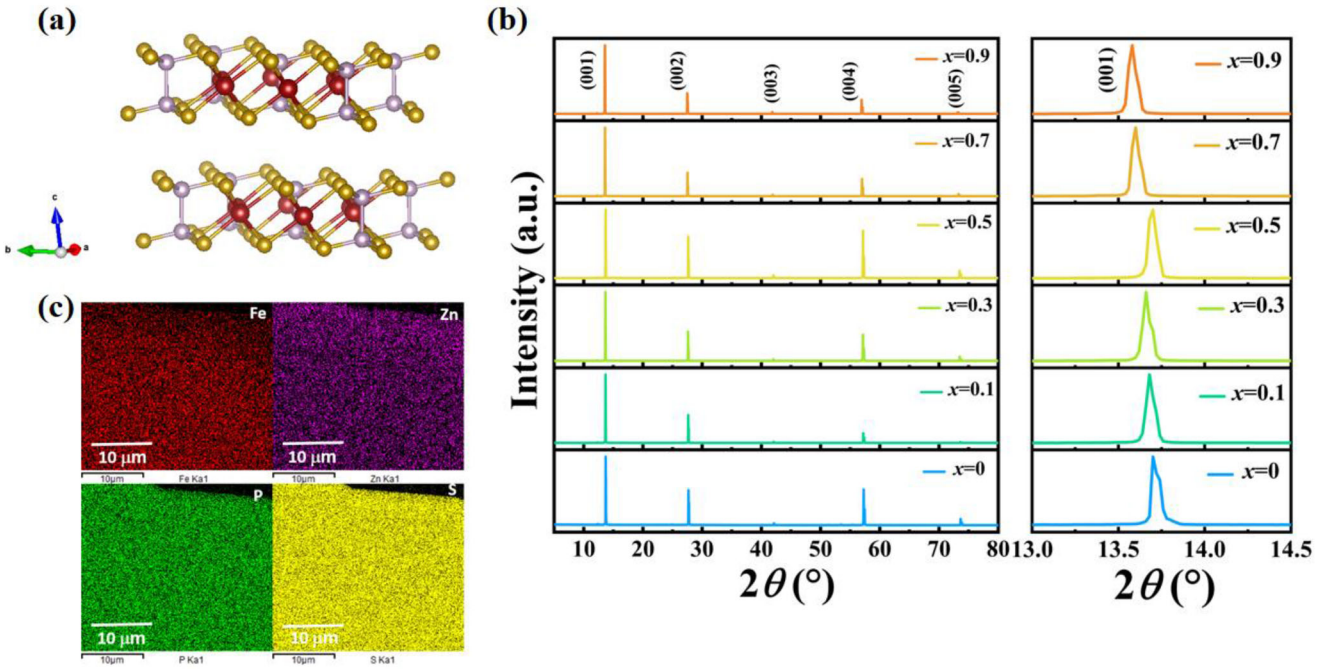

Figure 1. a) Illustration of MPX_3 crystal structure. M, P, and X atoms are represented by red, purple, and gold spheres. b) X-ray diffraction (XRD) patterns of $Fe_{1-x}Zn_xPS_3$ single crystals showing the (00L) reflections. Right panel: the shift of (001) diffraction peaks. c) Energy-dispersive spectroscopy (EDS) elemental mapping of $Fe_{0.5}Zn_{0.5}PS_3$.

center of the honeycomb ring. Layers are stacked along the trigonal axis via vdW forces.

While sharing isomorphic crystal structure, the MPX_3 system displays various antiferromagnetic (AFM) ground states. Bulk magnetic and neutron diffraction measurements show that MPX_3 with Mn, Fe, Co, Ni occupied at M site order antiferromagnetically at a temperature range between 78 and 155 K.[23–25] The magnetic structures below Néel temperature (T_N) decided by neutron scattering measurements turn to be Néel type for $MnPS_3$ and zigzag type for $FePS_3$, $NiPS_3$, and $CoPS_3$.[25–28] Néel type AFM refers to nearest-neighbor spins align in the opposite directions. In zigzag type antiferromagnetism, the spin states of the adjacent metal ions are parallel in a zigzag direction chain. Chains are coupled antiferromagnetically. Additionally, they exhibit distinct magnetic anisotropies. Mn^{2+} and Ni^{2+} have the electronic configurations $3d^5$ and $3d^8$, respectively. Their orbital degrees of freedom are quenched. The spin-orbit coupling is negligible, and compounds show virtually isotropic Heisenberg character. Of course, other interaction may also contribute to anisotropy. In $MnPS_3$, theoretic study indicates that dipole-dipole interaction gives rise to the weak single-ion anisotropy.[29] This compound can be described as XY type.[30] Fe^{2+} and Co^{2+} with the electronic configurations $3d^6$ and $3d^7$ have partially quenched orbital degrees of freedom. The spin-orbit coupling contributes to the magnetic anisotropy resulting in the Ising-type and XXZ-type antiferromagnets, respectively.[28,31] According to Mermin-Wager theory, introduction of anisotropy can stabilize the 2D magnetic order. Raman spectroscopy suggests that the magnetism in $FePS_3$ persists down to monolayer, making it the most promising candidate for spintronic applications.[32] In $FePS_3$, each Fe^{2+} is surrounded by six S^{2-}, forming a trigonal distorted octahedral. Under octahedral crystal field with weak-field limit, $3d$ orbital splits into doublet high energy e_g orbital and triplet low energy t_{2g} orbital. With trigonal distortion, t_{2g} orbital further splits into doublet E_g orbital and singlet A_{1g} orbital. Magnetic and neutron scattering measurements found that it is in high spin state with $S = 2$.[28] Fitting of neutron scattering data showed that the anisotropy behavior of $FePS_3$ can be best described by Ising model with a large single-ion anisotropy energy $\Delta = 2.66$ meV.[28] The magnetic structure below T_N is confirmed to be zigzag type with spin directions perpendicular to *ab* plane as shown in **Figure 2**a. Theoretically, for a honeycomb lattice, the magnetic structure is determined by the competition between nearest neighbor (NN) exchange interaction J_1, second nearest neighbor (SNN) exchange interaction J_2, third nearest neighbor (TNN) exchange interaction J_3, and interlayer exchange interaction J'. The illustrations of intralayer exchange interactions are shown in Figure 2b. NN exchange interactions have two components, direction interactions between metal ions and superexchange interactions via S ions [Fe(1)-S(1)-Fe(2)]. Le Flem et al. demonstrated that the direct exchange between Fe^{2+} should be ferromagnetic.[33] Goodenough-Kanamori rule suggests that the superexchage interaction of Fe^{2+}-S-Fe^{2+} in the present configuration is also ferromagnetic. These analyzes are consistent with inelastic neutron spectroscopy. J_1 is 1.46 meV from fitting.[28] J_2 purely comes from superexchange with two sulfur ions on the route, for example Fe(1)-S(1)-S(3)-Fe(3) as displayed in Figure 2c. However, S(1) is above the Fe plane and S(3) is below the plane. This path is deeply unlike. Experimental results also demonstrate that J_2 is very weak (−0.04 meV).[28] The TNN interaction J_3 has a promising pathway: Fe(1)-S(1)-S(2)-Fe(4). Both theoretic and experimental studies show that it is strong and AFM (−0.96 meV).[28,33] J_3

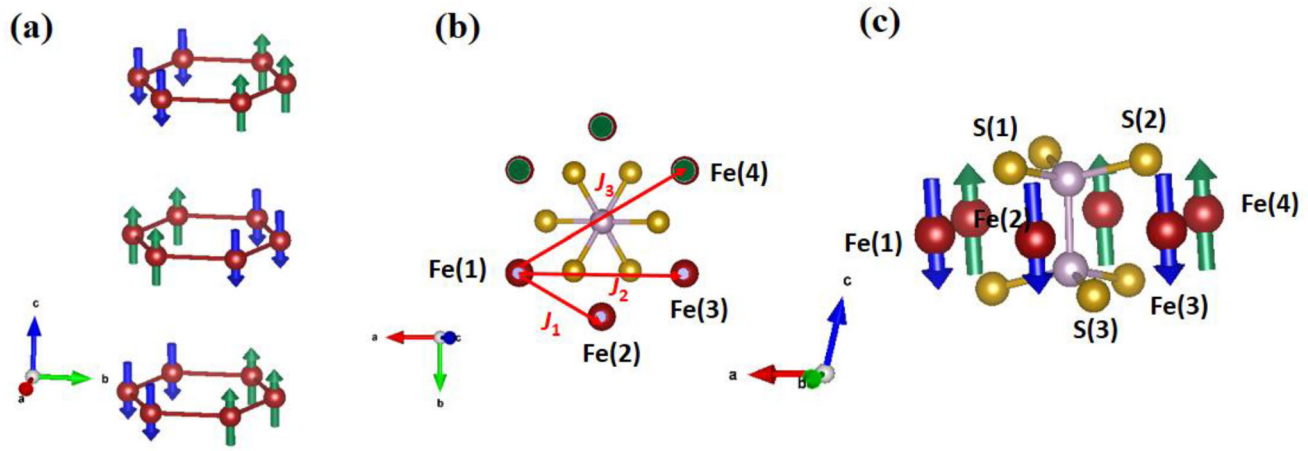

Figure 2. a) Side view of $FePS_3$ magnetic structure. Two different moment orientations are color-coded. b) Top view of $FePS_3$ magnetic structure. Selected Fe atoms are marked with numbers. NN, SNN, and TNN superexchange interactions are listed as J_1, J_2, and J_3, respectively. c) Side view of $FePS_3$ magnetic structure within single layer. Selected Fe and S atoms are marked with numbers.

is thought to be the most decidable interaction for the magnetic order. The interlayer exchange interaction J' is nearly negligible (−0.0073 meV).[28] Another parent compound $ZnPS_3$ is nonmagnetic with similar crystal structure and lattice parameters of $FePS_3$.[24,34]

For spintronic applications, manipulation of the spin state by tailoring the strength of exchange interactions, as well as single-ion anisotropy, is crucial. The aim is to induce non-zero net magnetization at higher ordering temperature. Various strategies have been implemented by introducing defects, intercalation, substrate, and chemical doping. Previous attempts focused on $Mn_{1-x}Fe_xPSe_3$,[35] $Mn_{1-x}Fe_xPS_3$,[36,37] $Fe_{1-x}Ni_xPS_3$,[38,39] and $Mn_{1-x}Ni_xPS_3$[40,41] solid solutions for which two end members have distinct spin anisotropies, spin directions, and magnetic interactions. Glassy-like states, such as magnetic glass, spin glass/cluster spin glass, are observed with the ordering temperatures falling between the Néel temperatures of two parent compounds. Recently, Wang et al. report sulfur defect induced weak ferromagnetism in $Ni_{1-x}Co_xPS_3$ nanosheets.[42] Ma et al. report a ferrimagnetic phase in 1,10-phenanthrolne intercalated $Fe_xNi_{1-x}PS_3$ samples due to Fe vacancy.[43] In this work, we report the first dopant-induced ferromagnetism in Zn^{2+} doped $FePS_3$ system.

2. Results and Discussion

2.1. Structure and Composition Characterization of $Fe_{1-x}Zn_xPS_3$

The phases of $Fe_{1-x}Zn_xPS_3$ solid solutions were characterized by XRD as shown in Figure 1b. All peaks can be indexed by (00L) diffraction peaks of space group $c2/m$. No impurity phase was detected. The shifts of most intense (001) peaks indicate successful alloying of Zn into $FePS_3$ single crystals. The successful intercalation of Zn was also confirmed by energy dispersive spectroscopy (EDS) measurements. The element mapping (Figure 1c) shows uniform distributions of Fe, Zn, P, and S ions.

2.2. FM State Induced by Non-Magnetic Dopants

The temperature dependent DC susceptibilities for $Fe_{1-x}Zn_xPS_3$ series are shown in **Figure 3**. Six compositions ($x = 0, 0.1, 0.3, 0.5, 0.7, 0.9$) are measured with both zero field cooling (ZFC) and field cooling (FC) sequences. Left panel displays susceptibility curves for magnetic field applied parallel to ab plane ($\chi_{II}(T)$). Right panel exhibits susceptibility curves for magnetic field applied perpendicular to ab plane ($\chi_{\perp}(T)$). Since Fe is the only element in the chemical formula that contributes to magnetization, the unit of susceptibility is converted to emu/Fe mol Oe. In general, these compositions can be divided into three groups.

The first group contains $FePS_3$ and $Fe_{0.9}Zn_{0.1}PS_3$ ($x = 0.1$). In the paramagnetic state, with decreasing temperature, susceptibilities increase due to suppressed thermal fluctuations. Broad maximums in both $\chi_{II}(T)$ and $\chi_{\perp}(T)$ are obtained at $T_{max} = 128$ and 110 K for $FePS_3$ and $Fe_{0.9}Zn_{0.1}PS_3$, respectively. Broad maximums have been observed previously in layered AFM material such as $MnTiO_3$ and K_2NiF_4. Neutron scattering measurements indicate very long-range correlation within plane, but no correlations between the planes below T_{max}.[44,45] Inflection points are observed in both $\chi_{II}(T)$ and $\chi_{\perp}(T)$ curves at temperatures just a few degrees below T_{max}, which reflects the onset of 3D long-range order. The temperatures of these inflection points are defined as the *Néel* temperature $T_N = 122$ K and 102 K for $FePS_3$ and $Fe_{0.9}Zn_{0.1}PS_3$, respectively. Additionally, the $\chi_{\perp}(T) > \chi_{II}(T)$ behavior for the high temperature paramagnetic region, and $\chi_{\perp}(T) < \chi_{II}(T)$ behavior for the low temperature AFM region. This indicates Ising-type magnetism with magnetic easy axis perpendicular to the ab plane. The susceptibility curves of parent compound $FePS_3$ are consistent with previous reports.[46]

For the second group of Zn doping level $x = 0.3$ and 0.5, the shapes of $\chi_{II}(T)$ and $\chi_{\perp}(T)$ are different. For $H_{II}ab$, the sharp PM to AFM transition turns to be mild, leaving only a bump at T_N. Separations between ZFC and FC curves are observed at lower temperatures, a character of spin glass, cluster spin glass or superparamagnetism. The irreversibility temperature is denoted T_{irr}. These irreversibility behaviors can be more obviously

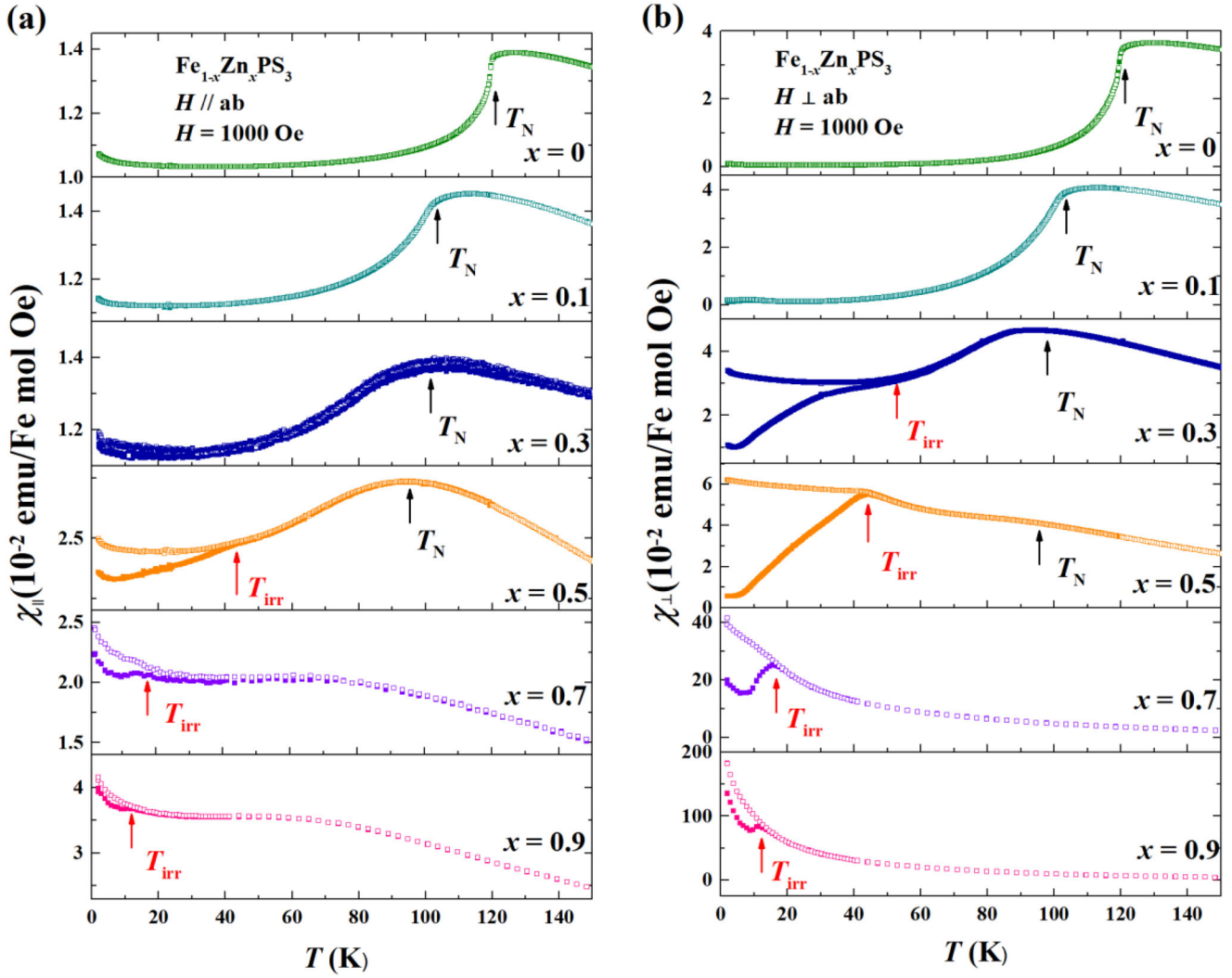

Figure 3. a) Magnetic susceptibilities of $Fe_{1-x}Zn_xPS_3$ ($x = 0$, 0.1, 0.3, 0.5, 0.7, and 0.9 from top to bottom) series under in-plane magnetic field of 1000 Oe. b) Magnetic susceptibilities of $Fe_{1-x}Zn_xPS_3$ ($x = 0$, 0.1, 0.3, 0.5, 0.7, and 0.9 from top to bottom) series under out-of-plane magnetic field of 1000 Oe. Black and red arrows indicate magnetic ordering temperature T_N and irreversibility temperature T_{irr}.

observed in $\chi_{\perp}(T)$. If we have a close-up view of $\chi_{\perp}(T)$ of $x = 0.3$, below T_N, the FC data first decreases and then increases at low temperature, distinct from the ZFC data which shows a monotonically decrease with lowering temperature. This is a hallmark of weak ferromagnetism associated with glassy behavior. For $\chi_{\perp}(T)$ of $x = 0.5$, the PM to AFM transition is virtually negligible.

In the third group ($x = 0.7$ and 0.9), the PM to AFM transitions are smeared out. $\chi_{II}(T)$ shows monotonically increase upon decreasing temperature although the magnitudes of them are comparable to compositions in group one and two. A weak splitting between ZFC and FC curves happens at low temperature (<20 K). On the other hand, the magnitudes of $\chi_{\perp}(T)$ get strongly enhanced at low temperature. For $x = 0.9$ sample, the absolute value of $\chi_{\perp}(T)$ in ZFC sequence reaches ≈1.5 emu/Fe mol Oe at 2 K, two orders larger than $\chi_{\perp}(T)$ in ZFC sequence of $FePS_3$ at 2 K. Of course, the ratio of $\chi_{\perp}(T)$ to $\chi_{II}(T)$ surges at low temperature. All these features indicate that the samples in this group are particularly close to long range ferromagnetic order with an out-of-plane easy axis.

To further explore the magnetic properties, the high temperature susceptibilities were fitted by Curie-Weiss law using equation

$$\chi = \chi_0 + \frac{C}{T - \theta_{CW}} \quad (1)$$

Since the strong anisotropic behaviors, fittings of $\chi_{II}(T)$ and $\chi_{\perp}(T)$ yield distinct results. The Curie-Weiss temperatures are listed in **Table 1** together with other magnetic parameters. With the increases of Zn dopants, Curie-Weiss temperature derived from $\chi_{\perp}(T)$ increase from −29.4 K for $FePS_3$ to −16.8 K for $Fe_{0.5}Zn_{0.5}PS_3$. At the same time, T_N gradually decreases. Both features imply a weakening of AFM correlations. When Zn concentration further increases to 0.7, θ_{cw} derived from $\chi_{\perp}(T)$ becomes positive, demonstrates the dominating role of FM correlation.

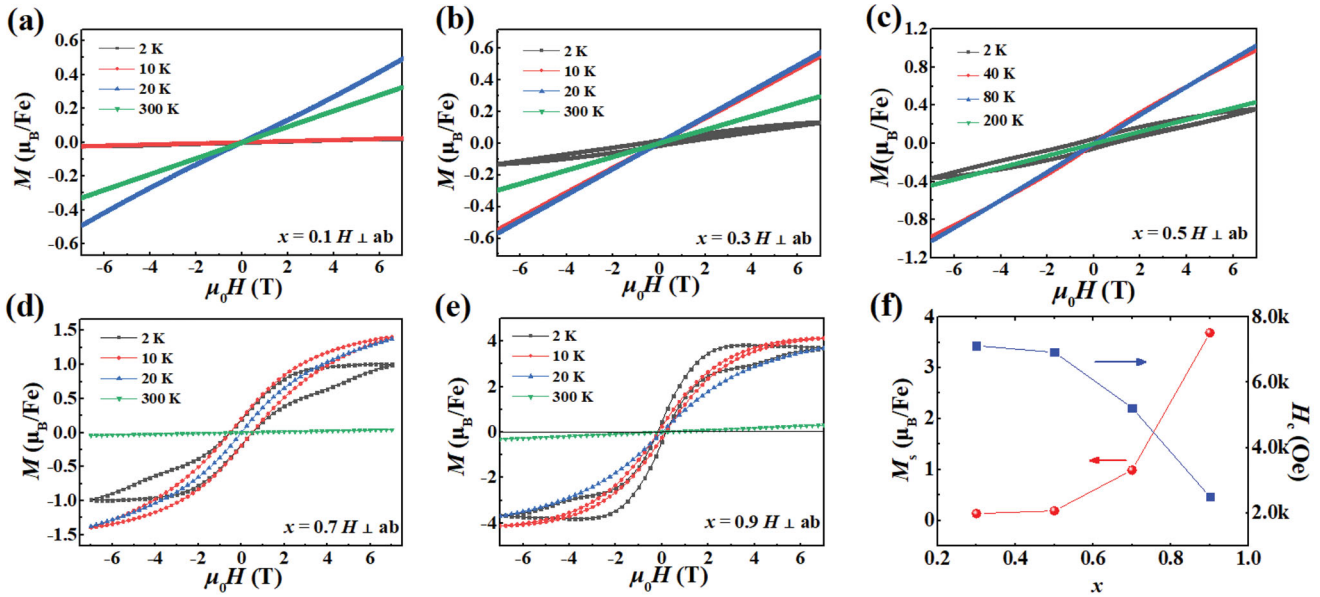

Figure 4. Isothermal magnetization for magnetic field applied perpendicular to *ab* plane for $Fe_{1-x}Zn_xPS_3$ a) $x = 0.1$, b) $x = 0.3$, c) $x = 0.5$, d) $x = 0.7$, and e) $x = 0.9$. f) Saturated magnetization taken at 2 K and 7 T and coercive field as a dependence of Zn doping concentration x.

Table 1. Selected magnetic parameters derived from DC susceptibility measurements under parallel or perpendicular external magnetic field of 1000 Oe for $Fe_{1-x}Zn_xPS_3$.

x (Zn)	T_N K	T_{irr} K	$\theta_{cw}(\chi_{II})$ K	$\theta_{cw}(\chi_{\perp})$ K	$\chi_{\perp}$(2K)II (emu/Fe mol Oe)
0	122	-	−231.1	−29.4	0.00096
0.1	102	-	−493.7	−26.6	0.0013
0.3	101	52.5	−771.4	−19.9	0.011
0.5	95	44	−496.8	−16.8	0.006
0.7	-	15.4	−119.9	35.1	0.19
0.9	-	11.6	−28.4	43.1	1.22

Meanwhile, the residue magnetization of $\chi_{\perp}(T)$ shows strong enhancement for $x \geq 0.7$.

Isothermal magnetization measurements were carried on all compositions with magnetic fields applied parallel and perpendicular to the *ab* plane. For *HIIab*, magnetization *M* shows linear dependence on field *H* at all compositions and temperature ranges as shown in supporting information. While for *H*⊥*ab*, with Zn doping content ≥ 0.3, hysteresis loops appear at low temperature, which hints at the onset of FM interactions. The hysteresis loops become pronounced for $x = 0.7$ and 0.9 samples as shown in **Figure 4**d,e. Note that for the $x = 0.7$ and 0.9 samples,hysteresis loops appear at temperatures above T_{irr}. They should not originate from glassy behavior. The magnetism of $x = 0.9$ sample saturates quickly at 2 K. The saturated moment reaches ≈4 μ_B/Fe. Saturated moments as well as coercive fields via Zn concentration x are plotted in Figure 4f. For the $x = 0.3$ and 0.5 samples, we take the moments measured at 2 K and 7 T as the saturated moments. As the Zn dopant is increased, the saturated magnetic moment gradually increases while coercive field decreases correspondingly.

To further explore the magnetic ground states below T_{irr}. Thermoremanent magnetization measurements under field applied perpendicular to *ab* plane are performed on samples with Zn dopants ≥ 0.3 (**Figure 5**a). Significant relaxation is observed. These curves can be nicely fitted by a stretched exponential decay function:

$$M(t) = M_0 + M_r e^{\left[-(t/\tau)^{1-p}\right]} \quad (2)$$

Here, M_0 denotes the static ferromagnetic component, M_r relates to the dynamic glassy component. τ is the relaxation time. p falls into the range between 0 and 1 for typical spin glass or cluster glass. The case $p = 0$ corresponds to Debye exponential relaxation, while $p = 1$ indicates no relaxation at all. Refinement results are shown in Figure 5b. The relaxation times grow exponentially with increase of Zn concentration. At the same time, p increases from 0.5 to ≈1 for $x = 0.9$. Both parameters demonstrate that the $Fe_{0.1}Zn_{0.9}PS_3$ compounds are particularly close to the static order.

2.3. XPS Studies

The valence states are investigated using XPS. As shown in **Figure 6**c, the peaks at 1022.7 and 1045.7 eV can be assigned to 2+ valence state for Zn $2p_{3/2}$ and $2p_{1/2}$, respectively. Figure 6d,e also indicate the valence states of P and S to be 4+ and 2-, respectively. Figure 6a,b show the Fe 2p core level spectra for $Fe_{0.1}Zn_{0.9}PS_3$ and $Fe_{0.3}Zn_{0.9}PS_3$, respectively. Data quality are limited by the low Fe concentration and the low conductivity of the samples. The Fe 2p core level spectrum of $Fe_{0.3}Zn_{0.7}PS_3$ sample has a better resolution. The deconvolution of Fe 2p core level yields two

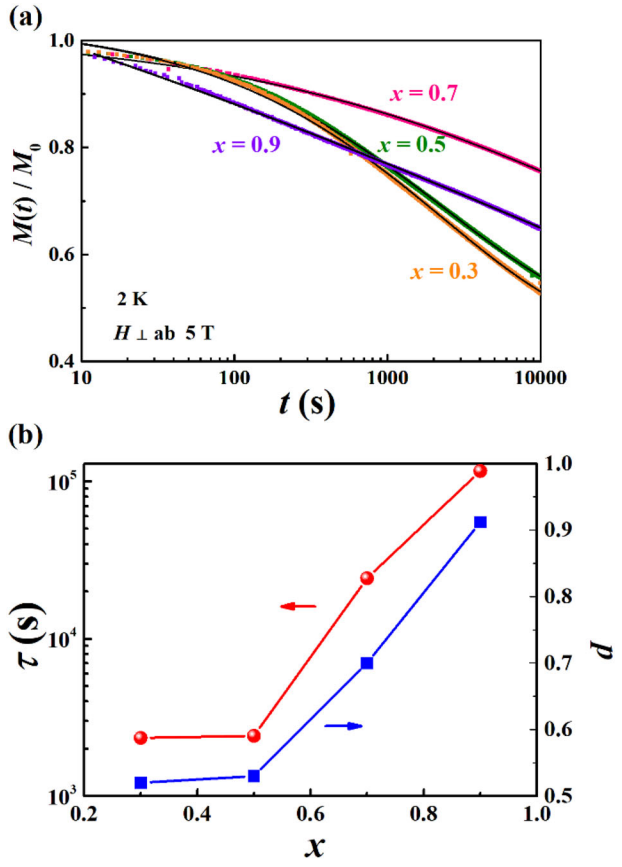

Figure 5. a) Time-dependent normalized thermoremanent magnetization measured at 2 K for $x = 0.3$, 0.5, 0.7, and 0.9 samples of $Fe_{1-x}Zn_xPS_3$. The black solid lines are fitting curves. b) Relaxation time τ and parameter p derived from fittings.

major bumps (Fe $2p_{3/2}$, Fe $2p_{1/2}$), encompassing a set of two Fe $2p_{3/2}$ (708.4 eV, 710.9 eV) peaks and two Fe $2p_{1/2}$ (721.5 eV, 724.0 eV) peaks. The peaks at 708.4 and 721.5 eV are assigned to the 2+ valence state of Fe $2p_{3/2}$ and $2p_{1/2}$, respectively. The peaks at 710.9 and 724.0 eV are attributed to the 3+ valence state of Fe $2p_{3/2}$ and$2p_{1/2}$, respectively. For Fe^{3+} and high spin state of Fe^{2+}, satellite features will be observed. Broad structures at 714.5 and 729.4 eV are attributed to them. The additional 3+ valence state of Fe indicates the introduction of holes into the samples.

2.4. Discussion

From the above comprehensive magnetic measurements, we can conclude that Zn doping in general weakens the AFM correlation. For *H*⊥*ab*, weak ferromagnetism associated with spin/cluster spin glass emerges at 30% Zn doping. With further increase of the Zn content, the relaxation time increases while freezing temperature of glass state decreases. The ground state of the 90% Zn doped sample is very close to the static FM order. For *H*II*ab*, there are no traces of ferromagnetism. These observations are counterintuitive since that Zn^{2+} is nonmagnetic. To clarify the underlying mechanism of the FM order in Zn-rich samples, we performed first principles density functional theory (DFT) calculation on the composition showing ferromagnetism. Since in our experiments the ferromagnetism appears in compositions close to $ZnPS_3$, we first check this end member. The DFT optimized lattice constants are very close to the experimental one.[47] The calculated band structure shows that $ZnPS_3$ is a semiconductor with an indirect bandgap ≈2 eV as shown in Figure S2, Supporting Information, which is also consistent with the previous calculations.[47,48] All these results provide a reliable starting point for the following calculations.

Then in a $2 \times 1 \times 1$ or $1 \times 1 \times 2$ supercell (as shown in **Figure 7**a,b), one of eight Zn is replaced by one Fe, resulting in a Fe doping concentration of 12.5%, close to the experimental 10% (Fe) case. The energy difference between these two configurations are very small (≈1 meV), and all physical properties of them are very similar as expected. The calculated density of states demonstrates a spin polarized semiconductor, with total magnetic moment 4 μ_B. Despite the large moment of Fe dopant (3.63 μ_B) as shown in Figure S3, Supporting Information, the neighboring S ions also contribute the magnetization slightly, due to *p-d* orbital hybridization, as shown Figure 6c,d.

We also studied the magnetic anisotropy of above $2 \times 1 \times 1$ and $1 \times 1 \times 2$ supercell as listed in Table S1, Supporting Information. The energy *E*(c) with spin pointing along the *c**-axis (out-of-plane direction) is always the lowest one: 0.7 meV lower than *E*(b) and 1.6 meV lower than *E*(a). Therefore, in the Zn-doped $FePS_3$, the Ising-type anisotropy does not change. Ferromagnetism may be present in its monolayer limit.

To further studied the interaction between Fe ions, appended DFT calculations are performed on a $2 \times 1 \times 2$ supercell with two Fe dopants, by keeping the Fe doping concentration of 12.5%. Two Fe dopants' configurations are adopted. For the first one, two Fe dopants are placed at adjacent layers as shown in **Figure 8**a. For the other, two Fe dopants are SNN to each other as shown in Figure 8b. The energies are calculated for both FM and AFM orders. For both configurations, the energy difference between FM and AFM orders, which is E_{FM}-E_{AFM}, are positive, as shown in Figure 8c,d, suggesting an AFM ground state. This is actually not surprising since that the doped compound is still highly insulating. No impurity bands form around the Fermi level. Our XPS measurements demonstrate that holes are introduced by Fe dopants. We then calculated the energies of the FM and AFM orders with tiny hole doping. For both Fe dopants' configurations, the FM state can be stabilized by tiny hole doping. The energy difference E_{FM}-E_{AFM} decreases linearly with hole concentration, as shown in Figure 8c,d.

DFT calculations demonstrate the essential role of the hole concentration introduced by the Fe dopants in $ZnPS_3$ to the FM order. We then refer to the situations of diluted magnetic semiconductors (DMS). In 3D DMS, ferromagnetism can emerge in oxides, nitrides, and III–V semiconductors. For example, 9% Mn doped GaN and 5% Fe doped ZnO display long range FM order.[49,50] In 2D DMS, Mn, Fe, Co, Ni-doped transition metal dichalcogenides, and Co-doped graphitic ZnO (gZnO) also display long range ferromagnetic order.[50,51] The percolation model of bound magnetic polarons (BMP) was used to understand the long-range ferromagnetic order in a few percent of magnetic ions doped non-magnetic oxides, which could not be explained by conventional super-exchange or double-exchange interactions.[52,53] The exchange interactions between shallow donor electron/hole

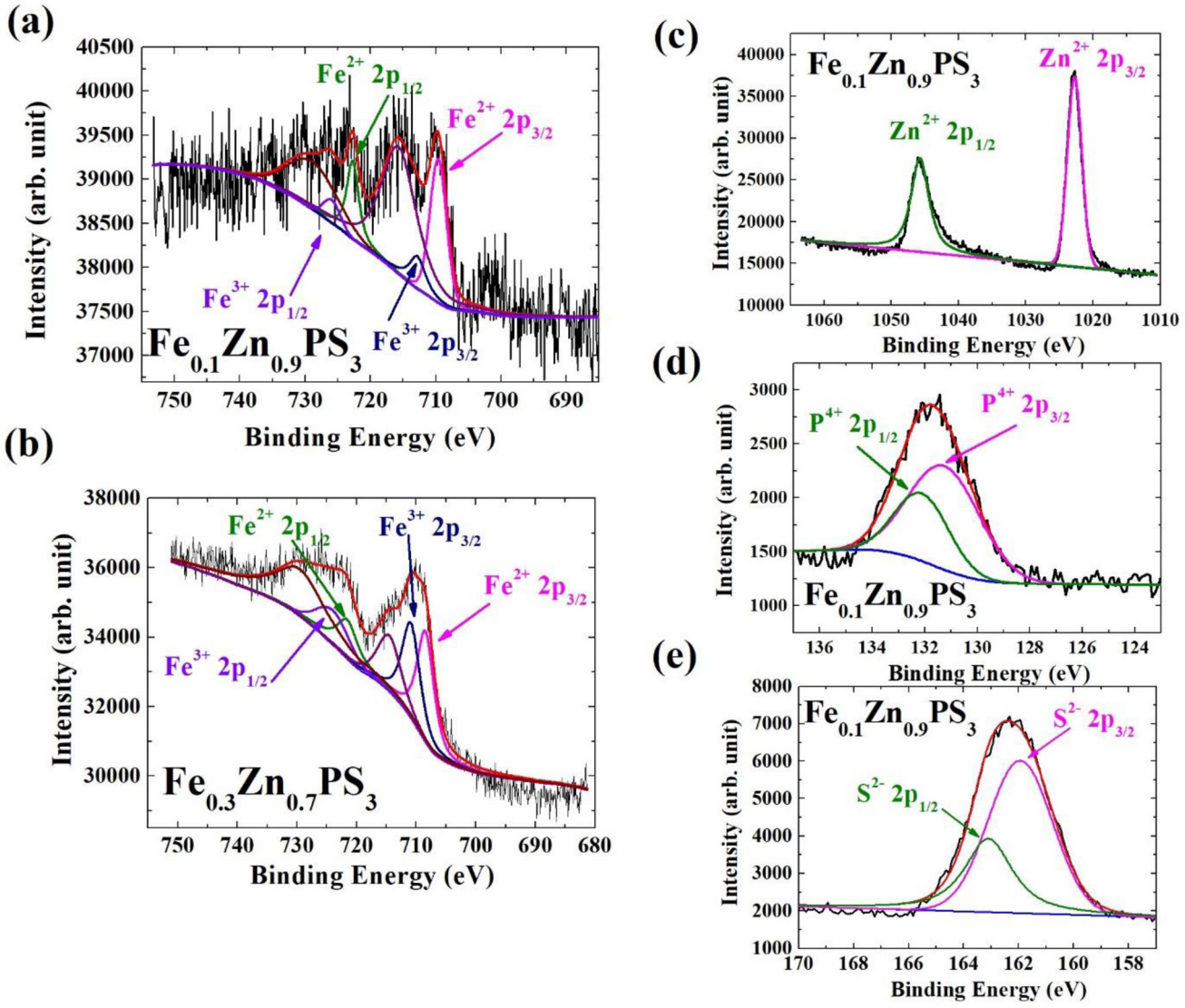

Figure 6. XPS spectra of a) Fe 2p core level, c) Zn 2p core level, d) P 2p core level, and e) S 2p core level for $Fe_{0.1}Zn_{0.9}PS_3$. b) XPS spectra of Fe 2p core level for $Fe_{0.3}Zn_{0.9}PS_3$.

and magnetic ions form BMP. These interactions are ferromagnetic when the 3*d* shell is less than half-filled, and AFM when the 3*d* shell is equal or more than half-filled. Considering two neighboring polarons overlapping with each other, the energy minimum is reached when the spins of the two donor electrons/holes are parallel. As the density of donor electrons/holes increases, percolation occurs at a concentration (named as polaron percolation threshold) much less than the magnetic ions cation threshold. The system reaches a ferromagnetic state where the spins of all donor electrons/holes are parallel to each other, and all magnetic ions' spins are parallel to each other.

The percolation model of BMP can well explain the evolution of magnetic properties in $Fe_{1-x}Zn_xPS_3$. We follow the assumption made in Co-doped gZnO thatone donor electron/hole can interact with about 10 magnetic ions. Long-range ferromagnetic order occurs when holes' concentration reaches 10% of magnetic ions cation percolation threshold. AFM order occurs for Fe concentration above magnetic ions cation percolation threshold.[54] Theoretic study revealed that the critical concentration of long range order for 2D honeycomb lattice with only NN interaction should be 0.7 (magnetic ion concentration).[55] The percolation threshold may be lower if SNN and TNN are also counted. For example, in Zn doped $MnPS_3$ system, the AFM long-range order persists until Mn concentration below 45%.[56–60] As stated in the introduction part, TNN turns out to be the decidable interaction in $FePS_3$.[28] The percolation threshold should be lower than 0.7 (magnetic ion concentration). In our case, with high Fe concentrations (e.g., x(Fe)≥0.5), the NN and TNN superexchange interactions can result in an AFM ground state. At low Fe concentration (x(Fe) ≈ 0.1), the ferromagnetism can be understood based on this BMP model. The competition between BMP induced impurity-band-exchange and superexchange are also responsible for the glassy behaviors of intermediate compounds.

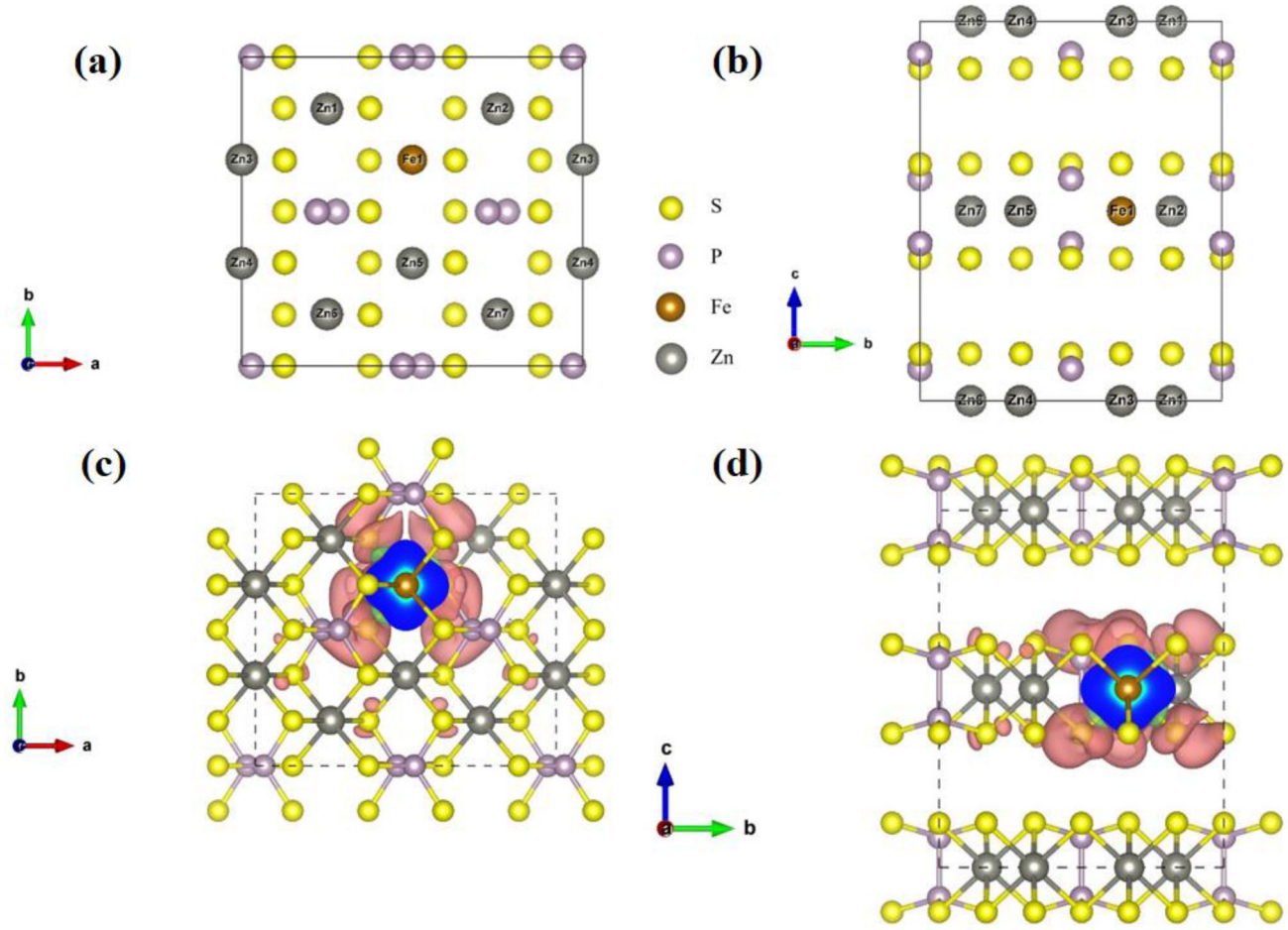

Figure 7. DFT calculation of 12.5% Fe doped $ZnPS_3$ in two configurations. Gold, grey, yellow, and purple balls represent Fe, Zn, S, and P, respectively. a) Structure of 2 × 1 × 1 supercell. b) Structure of 1 × 1 × 2 supercell. c,d) Corresponding distribution of spin density. The net magnetization is mostly contributed by the Fe dopants, while the neighboring S ions are also involved.

Another matter of debate is the microscopic image of magnetic ground state. How does ferromagnetism coexist with glassy behavior? What is the domain structure? Can this ferromagnetism persist to the mono layer? Further experiments including neutron diffraction, magnetic force microscope, magneto-optic Kerr microscope on few or mono-layer samples are desirable to answer these questions.

3. Conclusion

We have successfully grown high-quality single crystalline $Fe_{1-x}Zn_xPS_3$. Bulk magnetic measurements show that Zn doping weakens AFM correlations. Weak ferromagnetism associated with spin/cluster spin glass appears at 30% Zn doping. The relaxation time diverges as the Zn doping concentration increases to 90%, indicating an approach to static FM order. XPS measurements indicate the introduction of holes in samples with ferromagnetism. DFT calculations of the 87.5% Zn doped composition confirm a spin polarized state of Fe and adjacent S ions. It also demonstrate the essential role of hole concentration for the stabilization of ferromagnetism. BMP induced impurity-band-exchange interaction is used to explain the FM order. Its competition with superexchange interaction can reproduce the evolution of magnetic properties in the $Fe_{1-x}Zn_xPS_3$ series. Both bulk magnetic measurements and theoretical calculations support the Ising anisotropy in compounds with FM order, a prediction of the persistence of magnetic order in monolayer crystals. Our paper reports the first dopants induced ferromagnetism in Metal thio(seleno)phosphates series. It sheds new insight into magnetic instabilities in 2D vdW materials and possible routes to manipulate the spin states.

4. Experimental Section

Synthesis of $Fe_{1-x}Zn_xPS_3$ Single Crystals: $Fe_{1-x}Zn_xPS_3$ single crystals were grown via the chemical vapor transport method. Iron powder (99.9%), zinc granule (99.9%), sulfur powder (99.95%), and phosphorus chunks (99.999%) were mixed with stoichiometric ratio of chemical formula. The mixture was loaded into quartz tubes together with iodine as transport agent. All operations were carried in an argon-filled glove box. After being sealed under a pressure of 10^{-3} Pa, these tubes were heated in a two-zone tube furnace. The source and growth zone were heated to 700 and 650 °C, respectively, with a rate of 1 °C per minute and kept for 7 days.

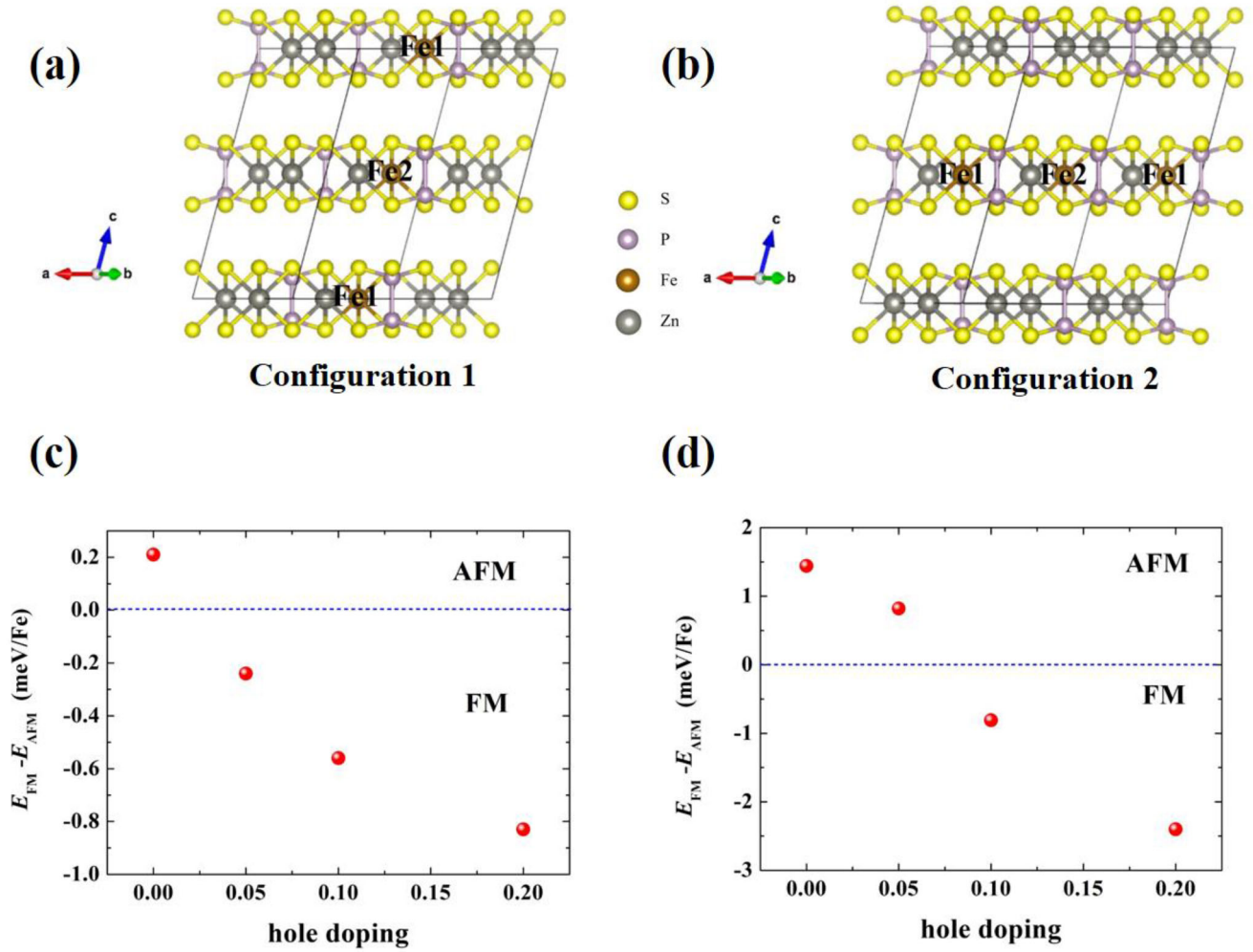

Figure 8. DFT calculation of 12.5% Fe doped $ZnPS_3$ in two Fe dopants' configurations. Gold, grey, yellow, and purple spheres represent Fe, Zn, S, and P, respectively. a) Structure of 2 × 1 × 2 supercell with two Fe dopants at adjacent layers with a distance of 6.78 Å. b) Structure of 2 × 1 × 2 supercell with two SNN Fe dopants at same layer with a distance of 5.97 Å. c,d) The energy difference between FM and AFM orders (E_{FM}-E_{AFM}) versus hole doping concentration.

Sample Characterization: As grown $Fe_{1-x}Zn_xPS_3$ single crystals were characterized via powder X-ray diffractometer (PXRD, Rigaku Smartlab3), scanning electron microscopy (Oxford INCA Energy) and EDS.

Magnetic Measurements: Bulk magnetic measurements were carried using SQUID magnetometer (Quantum Design). Temperature dependent DC susceptibilities were measured under a magnetic field of 1000 Oe with both ZFC and FC modes. Magnetic fields were applied at either parallel or perpendicular to *ab* plane. Isothermal magnetization measurements were also carried for field parallel and perpendicular to *ab* plane in a range of −7–7 T. Thermoremanent magnetizations were measured after ZFC to 2 K. Set a static magnetic field of 5 T for 300 s. Set the magnetic field to zero, then began the measurements.

XPS Measurements: XPS measurements were carried using Al *Kα* X-ray beam (1486.6 eV) with a current of 20 mA. Electron neutralizer were used to neutralize the positive charge created by X-ray source. C 1s spectrum was used for calibration.

Density Functional Theory Calculations: First-principles calculations were performed based on DFT as implemented in the Vienna ab initio simulation package.[61] The PBE parametrization of the generalized gradient approximation was used for the exchange-correlation functional.[62] During the structural relaxation, the convergence criterion for the energy was 10^{-6} eV for self-consistent iteration, and the Hellman-Feynman force was <0.01 eV $Å^{-1}$. The Hubbard *U* was applied using the Dudarev parametrization.[63] U_{eff} = 4 eV for Fe's 3*d* orbitals were used, which can lead to best agreement.[64] The energy cutoff was set as 400 eV. The *k*-point grid is 5 × 3 × 5, 6 × 3 × 3, and 3 × 3 × 3 for 2 × 1 × 1, 1 × 1 × 2, and 2 × 1 × 2 supercells, respectively. The vdW correction DFT-D3 method was adopted.[65,66]

Supporting Information

Supporting Information is available from the Wiley Online Library or from the author.

Acknowledgements

J.P. and X.Y. contributed equally to this work. The work at Southeast University was supported by the National Natural Science Foundation of China

(Grant nos. 11834002, 52130706) and the Fundamental Research Funds for the Central Universities (Grant nos. 2242022R10134, 3207022216A1). Work at Nanjing University was supported by the National Natural Science Foundation of China (Grant nos. 11834002, 51721001). Work at Hubei Normal University was supported by the National Natural Science Foundation of China (Grant no. 12074111). Work at Chinese Academy of Sciences and University of Science and Technology of China was supported by the National Natural Science Foundation of China (Grant no. U2032213). L.L. acknowledges support from Natural Science Foundation of Jiangsu Province (Grant no. BK20220797), and Open Research Fund Program of the State Key Laboratory of Low-Dimensional Quantum Physics (Grant no. KF202203).

Conflict of Interest

The authors declare no conflict of interest.

Data Availability Statement

The data that support the findings of this study are available from the corresponding author upon reasonable request.

Keywords

ferromagnetism, metal thio(seleno)phosphates, van der Waals material

Received: August 13, 2022
Revised: January 5, 2023
Published online: February 10, 2023

[1] K. S. Novoselov, A. K. Geim, S. V. Morozov, D. Jiang, Y. Zhang, S. V. Dubonos, I. V. Grigorieva, A. A. Firsov, *Science* **2004**, *306*, 666.
[2] L. Li, Y. Yu, G. J. Ye, Q. Ge, X. Ou, H. Wu, D. Feng, X. H. Chen, Y. Zhang, *Nat. Nanotechnol.* **2014**, *9*, 372.
[3] F. Xia, H. Wang, Y. Jia, *Nat. Commun.* **2014**, *5*, 4458.
[4] K. Watanabe, T. Taniguchi, H. Kanda, *Nat. Mater.* **2004**, *3*, 404.
[5] G. Cassabois, P. Valvin, B. Gil, *Nat. Photonics* **2016**, *10*, 262.
[6] L. Liu, J. Park, D. A. Siegel, K. F. McCarty, K. W. Clark, W. Deng, L. Basile, J. C. Idrobo, A. P. Li, G. Gu, *Science* **2014**, *343*, 163.
[7] Q. H. Wang, K. Kalantar-Zadeh, A. Kis, J. N. Coleman, M. S. Strano, *Nat. Nanotechnol.* **2012**, *7*, 699.
[8] M. Chhowalla, H. S. Shin, G. Eda, L.-J. Li, K. P. Loh, H. Zhang, *Nat. Chem.* **2013**, *5*, 263.
[9] K. S. Novoselov, A. Mishchenko, A. Carvalho, A. H. C. Neto, *Science* **2016**, *353*, aac9439.
[10] X. Y. Lin, W. Yang, K. L. Wang, W. S. Zhao, *Nat. Electron.* **2019**, *2*, 274.
[11] C. Gong, X. Zhang, *Science* **2019**, *363*, eaav4450.
[12] M. Bonilla, S. Kolekar, Y. Ma, H. C. Diaz, V. Kalappattil, R. Das, T. Eggers, H. R. Gutierrez, M.-H. Phan, M. Batzill, *Nat. Nanotechnol.* **2018**, *13*, 289.
[13] B. Huang, G. Clark, D. R. Klein, D. MacNeill, E. Navarro-Moratalla, K. L. Seyler, N. Wilson, M. A. McGuire, D. H. Cobden, D. Xiao, W. Yao, P. Jarillo-Herrero, X. Xu, *Nat. Nanotechnol.* **2018**, *13*, 544.
[14] C. Yang, J. R. Feng, F. Lv, J. H. Zhou, C. F. Lin, K. Wang, Y. L. Zhang, Y. Yang, W. Wang, J. B. Li, S. J. Guo, *Adv. Mater.* **2018**, *30*, 1800036.
[15] Z. Jiang, P. Wang, X. Jiang, J. Zhao, *Nanoscale Horiz.* **2018**, *3*, 335.
[16] Z. Fei, B. Huang, P. Malinowski, W. Wang, T. Song, J. Sanchez, W. Yao, D. Xiao, X. Zhu, A. F. May, W. Wu, D. H. Cobden, J.-H. Chu, X. Xu, *Nat. Mater.* **2018**, *17*, 778.
[17] Y. J. Deng, Y. J. Yu, M. Z. Shi, Z. X. Guo, Z. H. Xu, J. Wang, X. H. Chen, Y. B. Zhang, *Science* **2020**, *367*, 895.
[18] X. Jiang, Q. X. Liu, J. P. Xing, N. S. Liu, Y. Guo, Z. F. Liu, J. J. Zhao, *Appl. Phys. Rev.* **2021**, *8*, 031305.
[19] N. D. Mermin, H. Wagner, *Phys. Rev. Lett.* **1966**, *17*, 1133.
[20] K. Z. Du, X. Z. Wang, Y. Liu, P. Hu, M. I. B. Utama, C. K. Gan, Q. H. Xiong, C. Kloc, *ACS Nano* **2016**, *10*, 1738.
[21] R. Samal, G. Sanyal, B. Chakraborty, C. S. Rout, *J. Mater. Chem. A* **2021**, *9*, 2560.
[22] G. Ouvrard, R. Brec, J. Rouxel, *Mater. Res. Bull.* **1985**, *20*, 1181.
[23] R. Brec, *Solid State Ionics* **1986**, *22*, 3.
[24] Y. Takano, N. Arai, A. Arai, Y. Takahashi, K. Takase, K. Sekizawa, *J. Magn. Magn. Mater.* **2004**, *272*, E593.
[25] A. R. Wildes, V. Simonet, E. Ressouche, R. Ballou, G. J. McIntyre, *J. Phys.: Condens. Matter* **2017**, *29*, 455801.
[26] A. R. Wildes, V. Simonet, E. Ressouche, G. J. McIntyre, M. Avdeev, E. Suard, S. A. J. Kimber, D. Lançon, G. Pepe, B. Moubaraki, T. J. Hicks, *Phys. Rev. B* **2015**, *92*, 224408.
[27] A. R. Wildes, H. M. Ronnow, B. Roessli, M. J. Harris, K. W. Godfrey, *Phys. Rev. B* **2006**, *74*, 094422.
[28] D. Lançon, H. C. Walker, E. Ressouche, B. Ouladdiaf, K. C. Rule, G. J. McIntyre, T. J. Hicks, H. M. Rønnow, A. R. Wildes, *Phys. Rev. B* **2016**, *94*, 214407.
[29] C. Pich, F. Schwabl, *J. Magn. Magn. Mater.* **1995**, *148*, 30.
[30] A. R. Wildes, H. M. Ronnow, B. Roessli, M. Harris, K. W. Godfrey, *J. Magn. Magn. Mater.* **2007**, *310*, 1221.
[31] C. Kim, J. Jeong, P. Park, T. Masuda, S. Asai, S. Itoh, H.-S. Kim, A. Wildes, J.-G. Park, *Phys. Rev. B* **2020**, *102*, 184429.
[32] X. Z. Wang, K. Z. Du, Y. Y. F. Liu, P. Hu, J. Zhang, Q. Zhang, M. H. S. Owen, X. Lu, C. K. Gan, P. Sengupta, C. Kloc, Q. H. Xiong, *2D Mater.* **2016**, *3*, 031009.
[33] G. Leflem, R. Brec, G. Ouvard, A. Louisy, P. Segransan, *J. Phys. Chem. Solids* **1982**, *43*, 455.
[34] E. Prouzet, G. Ouvrard, R. Brec, *Mater. Res. Bull.* **1986**, *21*, 195.
[35] A. Bhutani, J. L. Zuo, R. D. McAuliffe, C. R. dela Cruz, D. P. Shoemaker, *Phys. Rev. Mater.* **2020**, *4*, 034411.
[36] T. Masubuchi, H. Hoya, T. Watanabe, Y. Takahashi, S. Ban, N. Ohkubo, K. Takase, Y. Takano, *J. Alloys Compd.* **2008**, *460*, 668.
[37] J. N. Graham, M. J. Coak, S. Son, E. Suard, J. G. Park, L. Clark, A. R. Wildes, *Phys. Rev. Mater.* **2020**, *4*, 084401.
[38] D. J. Goossens, S. Brazier-Hollins, D. R. James, W. D. Hutchison, J. R. Hester, *J. Magn. Magn. Mater.* **2013**, *334*, 82.
[39] R. R. Rao, A. K. Raychaudhuri, *J. Phys. Chem. Solids* **1992**, *53*, 577.
[40] Y. Shemerliuk, Y. Zhou, Z. Yang, G. Cao, A. U. B. Wolter, B. Büchner, S. Aswartham, *Electron. Mater.* **2021**, *2*, 284.
[41] Z. Y. Lu, X. Y. Yang, L. Huang, X. Y. Chen, M. F. Liu, J. Peng, S. Dong, J. M. Liu, *J. Phys.: Condens. Matter* **2022**, *34*, 354005.
[42] F. M. Wang, N. Mathur, A. N. Janes, H. Y. Sheng, P. He, X. L. Zheng, P. Yu, A. J. DeRuiter, J. R. Schmidt, J. He, S. Jin, *Sci. Adv.* **2021**, *7*, eabj4086.
[43] X. Ma, L. Zhang, C. Xu, Q. Dong, R. I. Walton, Z. Li, H. Shi, G. Chen, J. Hu, J. Li, H. Yang, *Chem. Commun.* **2020**, *56*, 4603.
[44] J. Akimitsu, Y. Ishikawa, Y. Endoh, *Solid State Commun.* **1970**, *8*, 87.
[45] R. J. Birgeneau, H. J. Guggenheim, G. Shirane, *Phys. Rev. Lett.* **1969**, *22*, 720.
[46] P. A. Joy, S. Vasudevan, *Phys. Rev. B* **1992**, *46*, 5425.
[47] A. J. Martinolich, C.-W. Lee, I. T. Lu, S. C. Bevilacqua, M. B. Preefer, M. Bernardi, A. Schleife, K. A. See, *Chem. Mater.* **2019**, *31*, 3652.
[48] N. Kurita, K. Nakao, *J. Phys. Soc. Jpn.* **1987**, *56*, 4455.
[49] S. Sonoda, S. Shimizu, T. Sasaki, Y. Yamamoto, H. Hori, *J. Cryst. Growth* **2002**, *237*, 1358.
[50] S. J. Han, T. H. Jang, Y. B. Kim, B. G. Park, J. H. Park, Y. H. Jeong, *Appl. Phys. Lett.* **2003**, *83*, 920.
[51] B. Li, T. Xing, M. Zhong, L. Huang, N. Lei, J. Zhang, J. Li, Z. Wei, *Nat. Commun.* **2017**, *8*, 1958.
[52] J. M. D. Coey, M. Venkatesan, C. B. Fitzgerald, *Nat. Mater.* **2005**, *4*, 173.

[53] A. Kaminski, S. D. Sarma, *Phys. Rev. Lett.* **2002**, *88*, 247202.
[54] R. Chen, F. Luo, Y. Liu, Y. Song, Y. Dong, S. Wu, J. Cao, F. Yang, A. N'Diaye, P. Shafer, Y. Liu, S. Lou, J. Huang, X. Chen, Z. Fang, Q. Wang, D. Jin, R. Cheng, H. Yuan, R. J. Birgeneau, J. Yao, *Nat. Commun.* **2021**, *12*, 3952.
[55] V. K. S. Shante, S. Kirkpatrick, *Adv. Phys.* **1971**, *20*, 325.
[56] N. Chandrasekharan, S. Vasudevan, *Phys. Rev. B* **1996**, *54*, 14903.
[57] D. J. Goossens, T. J. Hicks, *J. Phys.: Condens. Matter* **1998**, *10*, 7643.
[58] D. J. Goossens, A. J. Studer, S. J. Kennedy, T. J. Hicks, *J. Phys.: Condens. Matter* **2000**, *12*, 4233.
[59] A. M. Mulders, J. C. P. Klaasse, D. J. Goossens, J. Chadwick, T. J. Hicks, *J. Phys.: Condens. Matter* **2002**, *14*, 8697.
[60] A. R. Wildes, B. Roessli, B. Lebech, K. W. Godfrey, *J. Phys.: Condens. Matter* **1998**, *10*, 6417.
[61] G. Kresse, J. Furthmüller, *Phys. Rev. B* **1996**, *54*, 11169.
[62] J. P. Perdew, K. Burke, M. Ernzerhof, *Phys. Rev. Lett.* **1996**, *77*, 3865.
[63] S. L. Dudarev, G. A. Botton, S. Y. Savrasov, C. J. Humphreys, A. P. Sutton, *Phys. Rev. B* **1998**, *57*, 1505.
[64] B. Gao, L. Lin, C. Chen, L. Wei, J. Wang, B. Xu, C. Li, J. Bian, S. Dong, J. Du, Q. Xu, *Phys. Rev. Mater.* **2018**, *2*, 084401.
[65] S. Grimme, *J. Comput. Chem.* **2006**, *27*, 1787.
[66] S. Grimme, J. Antony, S. Ehrlich, H. Krieg, *J. Chem. Phys.* **2010**, *132*, 154104.